# Prevalence of pretransition disordering in the rutile-to-CaCl$_2$ phase transition of GeO$_2$

G. Alexander Smith [1,*] Daniel Schacher [2,*] Jasmine K. Hinton [2] Daniel Sneed [3] Changyong Park [4]
Sylvain Petitgirard,[5] Keith V. Lawler,[1,†] and Ashkan Salamat [2,‡]

[1]*Department of Chemistry & Biochemistry, University of Nevada Las Vegas, Las Vegas, Nevada 89154, USA*
[2]*Department of Physics & Astronomy, University of Nevada Las Vegas, Las Vegas, Nevada 89154, USA*
[3]*Physical and Life Sciences, Physics Division, Lawrence Livermore National Laboratory, Livermore, California, 94550, USA*
[4]*HPCAT, X-ray Science Division, Argonne National Laboratory, Argonne, Illinois 60439, USA*
[5]*ETH Zürich, Department of Earth Sciences, 8092 Zürich Switzerland*

The ability to tailor a material's electronic properties using density driven disordering has emerged as a powerful route to materials design. The observation of anomalous structural and electronic behavior in the rutile to CaCl$_2$ phase transition in SnO$_2$ led to the prediction that such behavior is inherent to all oxides experiencing such a phase transition sequence [Smith *et al.*, J. Phys. Chem. Lett. **10**, 5351 (2019)]. Here, the ultrawide band gap semiconductor GeO$_2$ is confirmed to exhibit anomalous behavior during the rutile to CaCl$_2$ phase transition. A phase pure rutile GeO$_2$ sample synthesized under high-pressure, high-temperature conditions is probed using synchrotron diffraction and x-ray and optical spectroscopy under high pressure conditions. Density functional theory calculations show that the enthalpic barrier to displacing an oxygen along the $B_{1g}$ librational mode decreases with pressure leading up to the rutile to CaCl$_2$ phase transition. The band structure of the distorted state shows that such oxygen displacements form small polarons.

## I. INTRODUCTION

All group 14 dioxides can adopt a rutile structure, though in the case of CO$_2$ it is molecular [1] and the nonmolecular group 14 dioxides can undergo a high-pressure rutile to CaCl$_2$ phase transition [2–5]. For SiO$_2$, Landau theory predicts an important variation in the elastic constants leading to a substantial softening of the shear modulus about the rutile to CaCl$_2$ transition which should have a strong influence on SiO$_2$'s sound wave velocity and is of high relevance to interpret seismic reflectors in the earth's mantle [6,7]. The rutile to CaCl$_2$ transition in GeO$_2$ has been previously reported to occur at 26 GPa [2], intermediate between that of SiO$_2$ at 55 GPa and SnO$_2$ at 15.4 GPa [2,3,17]. The milder conditions for phase transformations in GeO$_2$ than SiO$_2$ has long been exploited by the Earth science community for systematic mineralogical substitution with silicate minerals [8]. This analogy between silicates and germanates has helped to build the mineralogical model of the Earth and constraining the origin of seismological discontinuities in the deep Earth's mantle. For example, the transformation of the spinel structure to post-spinel in the magnesosilicate perovskite to identify the boundary between the upper and lower mantle at 660 km depth [9].

The rutile phase of GeO$_2$ has been recently considered for its electronic properties in the burgeoning field of ultrawide band gap semiconductors (UWBG) [10]. Its 4.680-eV band gap [11] is in the UV-C region of the electromagnetic spectrum, which is ideal for making solar-blind photodetectors as well as light sources for pathogen inactivation in food and water treatment [12,13]. GeO$_2$ has also received attention as a potential passivator for Ge semiconductor technologies, but high temperature decomposition into GeO has lead to complications in the manufacturing process [14]. Thus Ge based semiconductor devices remain unpopular despite having superior bulk electron and hole mobilities over Si, integral to improving device performance as the physical size of modern transistors are reaching a limit of scaling [15]. Rutile GeO$_2$ is also predicted to be ambipolarly dopable through first-principles defect calculations by substituting group 13 cations in Ge sites to serve as an electron acceptor with ionization energies in the 0.45 to 0.5 eV range [16]. Such doping enables $p$-type conduction through the impurity band, allowing for a tuning of the band gap and design of application-tailored materials.

Recently, a fourfold increase in conductivity during the rutile-type ($P4_2/mnm$) to CaCl$_2$-type ($Pnnm$) transition was observed in the transparent conducting oxide SnO$_2$ [17]. The transition from the rutile to the CaCl$_2$ structure is a ferroelastic, second-order phase transition typically accompanied by a continuous volume change, and it can vary in pressure depending on the deviatoric stress and temperature [6,18]. The rutile to CaCl$_2$ phase transition is driven by the softening of the Raman active $B_{1g}$ octahedral librational mode, which with increased pressure allows for larger energetically accessible octahedral libration angles [7]. The anomalous conductivity observed during the rutile to CaCl$_2$ transition in SnO$_2$ is best attributed to a disordered, pretransition state with single atom

*These authors contributed equally to this work.
†keith.lawler@unlv.edu
‡salamat@physics.unlv.edu

displacements of the oxygen sublattice enabled by a reduced energetic barrier for displacement from the softened $B_{1g}$ librational mode. The oxygen displacements effectively decrease the band gap of the material before the transition to the $CaCl_2$ phase [17].

This behavior is predicted to be universal in oxide materials experiencing this phase transition rather than inherent to the chemistry of the charged species in the material. Understanding and controlling this phenomena will allow for a pressure mediated tuning of the optoelectronic properties of materials. Here, we evaluate the universality of the pretransition disordered state during the rutile to $CaCl_2$ phase transition for $GeO_2$ via spectroscopic, diffraction, and theoretical methods. We comment on the how the defects affect the electronic properties of a rutile oxide.

## II. METHODS

Samples of rutile $GeO_2$ were synthesised in a large-volume press under high-pressure and temperature conditions. Static high-pressure experiments were conducted using custom-designed diamond anvil cells (DAC). Helium was used as the pressure transmitting media (PTM) and pressure was controlled via a membrane for fine pressure resolution. Pressure was determined using the ruby fluorescence scale [19]. Raman spectroscopy experiments were carried out on a home-built design, utilizing Optigrate volume Bragg gratings for low frequency measurements.

X-ray absorption and diffraction measurements were performed at HPCAT (United States, APS, sector 16) and were acquired on the same sample sequentially at each pressure. X-ray diffraction (XRD) was performed axially ($\lambda = 0.3738$ Å), through the diamond anvil using Boehler-Almax conical design diamonds to allow for a 70° angle aperture. Diffraction data was integrated using DIOPTAS software and Rietveld analysis was performed using GSAS software. The calculated absorption length for $GeO_2$ was calculated by HEPHAESTUS software and was matched by acquiring x-ray absorption (XAS) measurements radially through the sample chamber by using beryllium as the gasket material. XAS was acquired on the Ge $K$ edge with energy scanned by 350 eV before the white line of 11.103 and 1 keV after using a bare silicon mirror to tune energy. Raw XAS data were reduced and analyzed using DEMETER and FEFF [20,21].

XAS spectra were fit using a window of 2.8 to 13.7 Å$^{-1}$, using $k$ weights of 1, 2, and 0.5 chosen to achieve a better fit. $S_0^2$ was determined by restraining the value to one and fitting all data, and then fitting only the amplitude reduction factor over all fits simultaneously. All data was then refit using the optimized value in a two shell fit, by fitting all values with the starting guess of $\Delta R = 0$, MSRD=0.001, and $\Delta E = 0$. All variables were fit, and then $\Delta R$ and MSRD values were fit for each shell. Finally $\Delta E$ was refined again. MSRD values were restrained to be equal of greater than zero. Both 1 and 2 shell fits were performed.

*Ab initio* density functional theory (DFT) simulations using VASP (Vienna *ab initio* simulation package) were used for structural optimizations and to determine the effect of pressure mediated defects [22–26]. The strongly constrained and appropriately normed (SCAN) meta-GGA functional

with Grimme's -D3 dispersion correction was used throughout [25,27–29]. Each simulation used a $\Gamma$ centered $k$-point grid with a 0.3 Å$^{-1}$ spacing [30]. The tetrahedron method with Blöchl corrections were used to integrate the Brillouin zone due to its high degree of accuracy for nonmetals [31]. Projector-augmented wave (PAW) PBE pseudopotentials were utilized for both Ge and O with valence configurations of $s^2 p^2$ and $s^2 p^4$, respectively [32,33]. Energy and force convergence parameters were set to a difference of $10^{-10}$ eV and $10^{-3}$ eV/Å, respectively. Structural optimizations were performed as two sequential optimizations then a final energy evaluation resetting the plane-wave basis set between each step to minimize the effect of Pulay stress. Band structure plots were created by re-determining the bands along the high symmetry points and lines of a simple orthorhombic cell using a fixed, preconverged charge density. Band structure and density of states plots were made using the SUMO package [34].

## III. RESULTS AND DISCUSSION

The Landau free-energy potential with respect to the motion of the $B_{1g}$ librational mode in rutile structures is expected to soften as a function of pressure [7], thus a defining feature of a group 14 dioxide's rutile to $CaCl_2$ phase transition should be the abrupt hardening of a previously softening $B_{1g}$ mode while the other vibrational Raman modes harden [17]. Figure 1(a) shows that the central frequency of the $A_{1g}$ mode exhibits the expected hardening by increasing linearly without any deviations from 1 to 30 GPa. Likewise, the $B_{1g}$ mode exhibits the expected softening from the onset of compression until a clear hardening is observed by 28.4 GPa. A linear fit to the softening range of the $B_{1g}$ mode remarks a transition pressure into the $CaCl_2$ phase of 27 GPa based on where the deviation from linearity first occurs. DFT optimizations of the rutile and $CaCl_2$ structures of $GeO_2$ across the same pressure range show the $CaCl_2$ phase becoming the enthalpically favorable phase by ~27 GPa [Fig. 1(b)]. According to the optimizations, the transition into the $CaCl_2$ structure should be accompanied by a small volume change, $< 0.2$ Å$^3$.

The XRD determined volume-pressure relation for compressed $GeO_2$ [Fig. 2(a)] roughly follows a third-order Birch-Murnaghan equation of state (EOS) up to 33.7 GPa. Closer inspection reveals the full data set EOS fit is in very tight agreement with the experimental data until 19.7 GPa, after which noticeable deviations from the fit occur [Fig. 2(a) inset]. As diffraction was collected in a He PTM, it is unlikely these distortions are due to nonhydrostaticity at these pressure conditions [36], but are rather the system experiencing pretransition disordering. By 29.6 GPa, the distortions appear to be relieved, indicating the system has transitioned into the $CaCl_2$ phase as confirmed by Rietveld analysis of the XRD data. A table containing the Rietveld refined lattices as a function of pressure may be found in Ref. [35]. The transition into the $CaCl_2$ phase is accompanied by a smaller than predicted volume drop of ~0.03 Å$^3$ according to a third-order Birch-Murnaghan EOS fit of just the undistorted rutile phase (0–19.7 GPa).

Fitting an EOS up until any distortion is observed ($\leqslant 19.7$ GPa) and up until the $CaCl_2$ phase is confirmed by
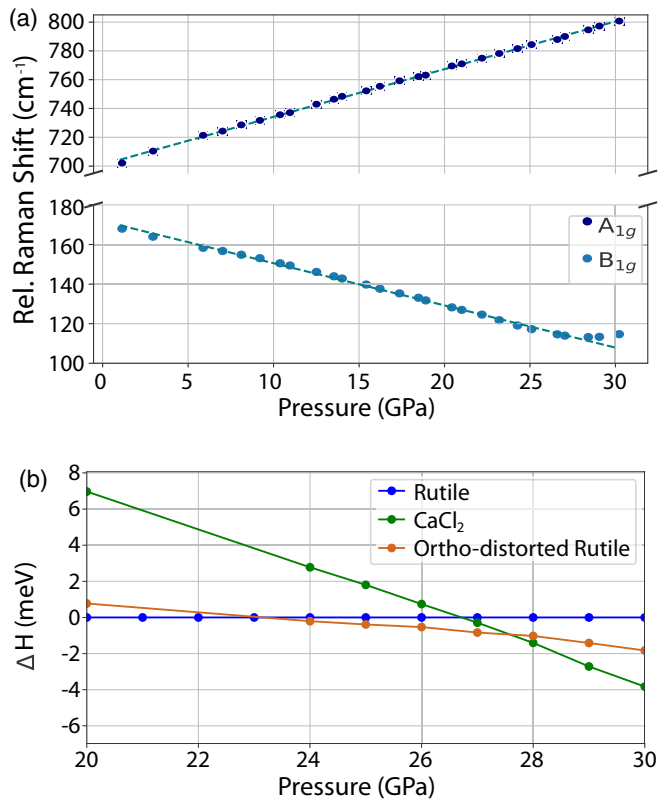
FIG. 1. (a) The central peak position from fitting the $A_{1g}$ and $B_{1g}$ Raman modes against pressure. Linear regressions have been added to both series to help guide the eye, as well as illustrate the $B_{1g}$ Raman mode's deviation from linearity around 27 GPa. (b) The enthalpy per unit cell of the rutile, $CaCl_2$, and orthorhombiclly distorted rutile phase as a function of pressure. All enthalpies are normalized to that of the rutile phase for a given pressure.

Rietveld analysis ($\leqslant$28.0 GPa) shows a marked 4% drop in the determined bulk modulus despite the latter fit encapsulating all of the data of the former (Table I). Extending the region of the 'pristine' rutile phase out to 21.5 GPa shows only a slight reduction to the fit bulk modulus showing that while disordering may be present by 21.5 GPa it only becomes significant at higher pressures. Oddly, the fit up to 28.0 GPa

TABLE I. Birch-Murnaghan equation of state fits across different pressure ranges. [a]The fit was done by fixing $V_0$ to that of the undistorted rutile (0–19.7 GPa) phase.

| Order | Pressure (GPa) | $V_0$ (Å$^3$) | $B_0$ (GPa) | $B_0$' |
|---|---|---|---|---|
|        | 0–19.7    | 55.45             | 231.83 | 6.46 |
|        | 0–21.5    | 55.45             | 231.18 | 6.55 |
| third  | 0–28.0    | 55.47             | 221.91 | 7.95 |
|        | 0–33.7    | 55.43             | 234.78 | 6.55 |
|        | 21.5–28.0 | 55.45[a]          | 239.19 | 6.17 |
|        | 0–19.7    | 55.38             | 254.77 |      |
|        | 0–21.5    | 55.38[a]          | 255.85 |      |
| second | 0–28.0    | 55.38[a]          | 262.78 |      |
|        | 0–33.7    | 55.38[a]          | 264.37 |      |
|        | 21.5–28.0 | 55.38[a]          | 265.44 |      |

shows a marked increase in the derivative of the bulk modulus, and a fit over just the 'disordered' region (21.5–28.0 GPa) shows an increase in the bulk modulus and a decrease in its derivative. These ambiguities are likely artifacts of the fit and can be alleviated by reducing the fit to that of a second-order Birch-Murnaghan equation of state with $V_0$ fixed to that of the pristine rutile phase ($\leqslant$19.7 GPa). In doing so, the bulk modulus is actually seen to increase for any set including data above 19.7 GPa (Table I). There is again only a slight difference if only the 21.5 GPa pressure point is included, but a much larger increase for the whole region that is driven by the data in the region between 21.5 and 28.0 GPa. Thus, there is a clear deviation from a crystalline rutile phase after 19.7 GPa, and disordering is present in $GeO_2$ by 21.5 GPa persisting at least until the transition into the $CaCl_2$ phase.

The difference in scattering intensity for Ge and O is small enough for reliable Rietveld identification of the lighter anion atomic positions, enabling accurate tracking of the Ge–O bond lengths within a coordination octahedra as a function of pressure [Fig. 2(b)]. The $GeO_6$ octahedra are initially irregular with an axial Ge–O distance of 2.01 Å and an in basal plane distance of 1.79 Å at 2.46 GPa. Only the basal Ge–O interactions are covalent according to covalent radii for Ge (1.20 Å) and O (0.66 Å) [37]. In line with this, the Ge–O bonds in the basal plane are seen to be very resistant to compression up to 20 GPa, while the axial ones are not. At 19.7 GPa, when the EOS fit for the rutile phase begins to break down, there is a clear indication of atomic disordering in $GeO_2$ from the sharp deviation in the pressure response of the bond lengths. As not all the oxygens are displaced in the pretransition disorded state, the result is an averaged out picture resulting in erratic behavior that increases as defect concentration grows but diminishes as the defects saturate. This deviation persists until $GeO_2$ has accessed the $CaCl_2$ phase, wherein the axial bond lengths increase and the basal lengths decrease with pressure. However, the DFT predicted structures state both Ge–O bond lengths should monotonically decrease with increased pressure, so there are residual defects even after the $CaCl_2$ phase transformation.

Extended x-ray absorption fine structure (EXAFS) spectroscopy probes the local coordination about an excited atom type providing complementary information to the equilibrium distances from electron densities discerned by diffraction. The average Ge–O distance within the first coordination shell of $GeO_2$ is obtained through fitting an x-ray absorption spectra through a two shell fit, and the resultant pressure response is shown in Fig. 2(d). The resolution of the EXAFS experiment is insufficient to resolve bond lengths beyond ~0.1 Å, in line with most modern EXAFS measurements, so axial and basal distances were not differentiated within a coordination shell [38,39]. In the rutile phase, there is a trend of decreasing average bond length within the first coordination shell with increasing pressure, in line with the diffraction and DFT data (DFT tables in Ref. [35]). EXAFS shows an earlier onset of disordering than XRD via the average bond lengths at 17.3 GPa and highlights disordering in the system. At 28 GPa, EXAFS shows a return to good agreement with the average crystallographic bond length before diverging again at higher pressures. The second cumulant of the EXAFS fit represents the mean squared relative displacement (MSRD) of the atoms,
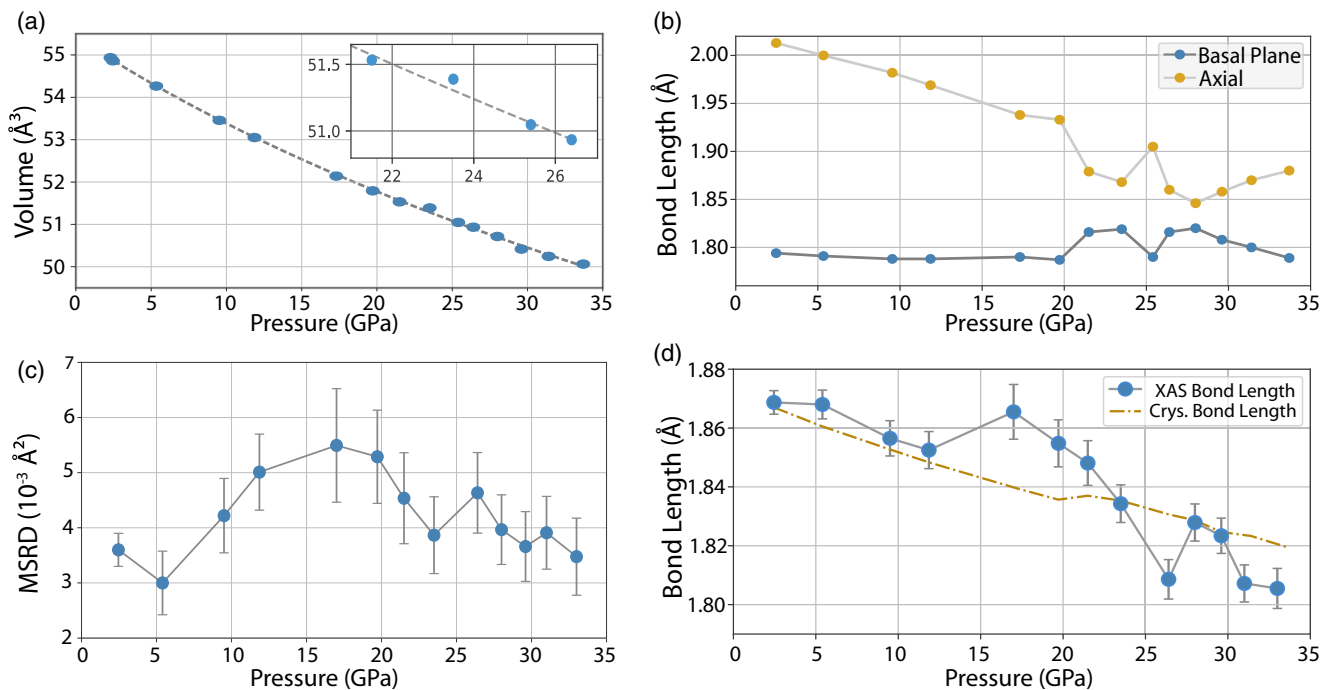
FIG. 2. A figure containing all x-ray techniques performed on GeO$_2$ in this study. (a) The pressure-volume response of the sample with a third order Birch-Murnaghan equation of state fit across all data to guide the eye. Note, there are at least two phases described by the data involved in said fit. The inset highlights deviations in the pretransition disordered state. (b) The average Ge–O bond lengths determined from Rietveld analysis. The error bars of both XRD panels are within the symbol size. (c) The mean squared relative displacement as measured by EXAFS. The strong response between 17 and 27 GPa is attributed to the pretransition disordered state. (d) The average Ge–O bond length determined from EXAFS with the weighted average crystallographic values.

which differs from mean squared displacement (MSD) that can be obtained from XRD in that the MSRD is relative to the atoms' instantaneous motion from each other, rather than their deviations from their crystallographic equilibrium position. This, while a small distinction, is significant as phonons often transverse in the same direction, however, this will not affect the MSRD as it is only affected by deviations relative to the scattering atom [40]. The $U_{iso}$ term from the XRD Rietveld refinement was fixed at 0.02 for all atoms and was not refined. Figure 2(c) shows the onset of disordering with a nearly factor of 2 increase of the EXAFS MSRD around 17.3 GPa from 5 GPa, which is in good agreement of disorder with the half path length. Taken as a marker of deviations of the perpendicular instantaneous average bond lengths, the initial rapid rise of the MSRD highlights the rapidly increasing librational angle as permitted by a rapidly flattening enthalpy landscape. Both EXAFS metrics indicate reordering following the initial maximum at 17.3 GPa.

The x-ray diffraction shows an abrupt return to the projected trend of pristine rutile phase at 25.4 GPa before deviating again. This indicates a return to an ordered state, driven by an increase in symmetrization in the oxygen positions. DFT predicts an orthorhombically distorted rutile phase to be stable around this pressure [Fig. 1(b)], yet the improvement in the statistical quality of fit metrics obtained by refining the XRD data with that structure is not sufficient to justify assigning the feature at 25.4 GPa to an orthorhombic rutile phase. Thus, at this pressure the difference between the rutile and CaCl$_2$ phases are at their minimum and will deviate from this pressure on. The anomalous behavior in the EXAFS

appears to quench around 28.0 GPa, wherein the average bond lengths return close to the rutile trend and the MSRD drops below that of the rutile phase. The EXAFS average bond lengths above 31 GPa are still below those anticipated by the average weighted crystallographic value determined by XRD. DFT predicts slightly longer bond lengths in the CaCl$_2$ phase, so these points as well as the overly short XAS determined bond lengths at 26.5 GPa indicate residual defects are present after the phase transformation.

The relative edge shifts of the XAS spectra (taken as the first critical point of the spectra) can be compared (Fig. 3)
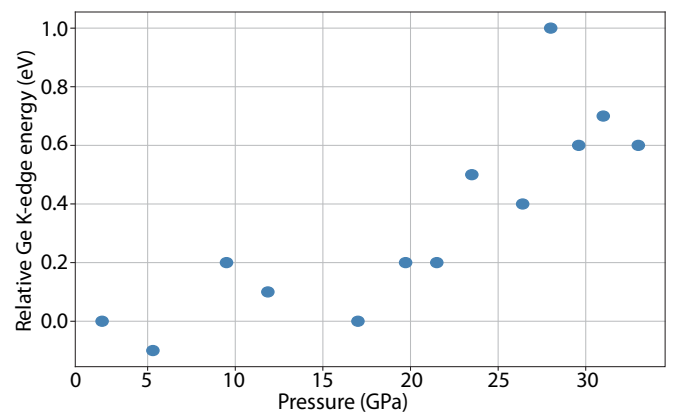


FIG. 3. The relative change in the Ge K-edge energy as a function of pressure. These energies were determined as the first critical point of the GeO$_2$ XAS spectrum.
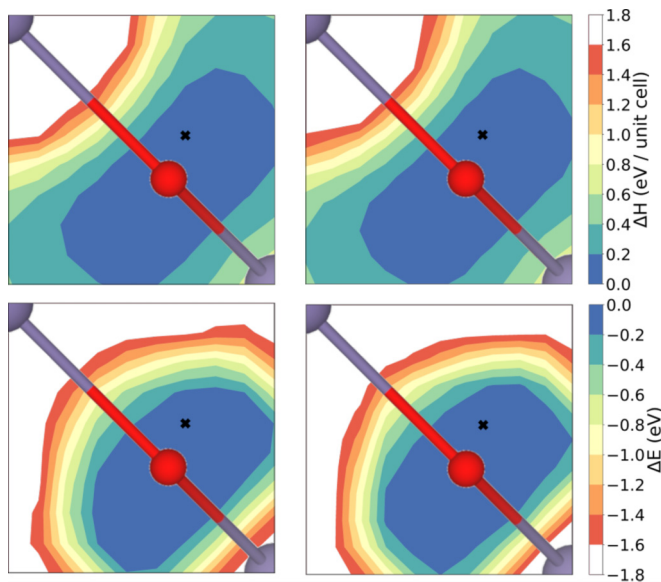
FIG. 4. The response in (top) enthalpy and (bottom) band gap associated with displacing an oxygen within its *ab* plane of a $3 \times 3 \times 3$ rutile supercell of $GeO_2$ at 20 GPa (left) and 25 GPa (right). Displacement by $11°$ relative to the rutile position (within grid resolution) marked with a black x.

to determine if any electronic response occurs as the material disorders. From 2.4 to 21.5 GPa, there is effectively no change in the edge energy indicating a consistent chemical environment of the system. However, there is a noticeable increase in edge energy at 23.5 GPa which persists to the highest pressure measured. Such an increase in edge energy is typically interpreted as an increase of the effective oxidation state of the target atom, implying that the presence of defects is driving some of the Ge atoms to a more ionic state. The increase in edge energy peaks just before the transition into the $CaCl_2$ phase at 28 GPa, indicating a peak concentration of defects in the sample. Following the transformation into the $CaCl_2$ phase the edge energy decreases while remaining above that of the low pressure rutile phases. While this is an expected effect as these types of oxides typically become more ionic with pressure, the values at the highest pressures still exceed the 0.01 eV/GPa growth rate of the edge energy observed up to 21.5 GPa. Transport measurements using an optometer were attempted to determine if any other electrical responses manifested due to the disordering (full details in Ref. [35]). Unfortunately, our setup is unable to detect in the sub-picoamp regime, so no useful signal was measured beyond 10 GPa.

To understand the deviations observed in the x-ray measurements, Fig. 4 shows the enthalpic and band gap response for the proposed disordering mechanism of displacing a single oxygen atom along the $B_{1g}$ librational mode within its respective *ab* plane in a $3 \times 3 \times 3$ supercell, i.e., a 0.91% defect density. In no case is the displacement more favorable than the base rutile structure, but at both pressures the oxygen can displace by 10%–20% along its librational path and still be within a potentially thermally accessible configuration with an $\Delta H \leqslant 100$ meV/unit cell. Increasing the defect density to 3.1% (a $2 \times 2 \times 2$ supercell, plot in Ref. [35]) transforms the

potential landscape into a steep well about the rutile position such that no significant displacements would be accessible. This confirms there is a low defect concentration at the outset of the disordering as indicated by the equation of state analysis measurements. Interestingly, increasing the pressure with a 0.91% defect density causes the well to become steeper at the edges, whereas the 3.1% defect density potential landscape flattens when pressure is increased. This shows that by 20 GPa the quartic nature of the free energy is saturated for low defect concentrations while it is beginning to transform away from a quadratic potential for higher defect concentrations. Both increased defect concentration and increased displacements are allowable with increased pressure, but the effects will be in competition with each other. Therefore the best explanation for what is observed experimentally is that a low concentration of defects with low displacements emerge around 20 GPa, the magnitude of the displacements increase with pressure, then at a certain pressure a several percent increase in defect concentration can be achieved at the cost of reducing the maximum displacement ($\sim$26 GPa), after which the magnitude of the displacements increase with pressure until the $CaCl_2$ phase change occurs.

Displacing an oxygen has some effect on the band gap of $GeO_2$, generally lowering it from its value in the pristine rutile state. The effect is minimal with a low defect concentration, not exceeding a 0.03 eV decrease within the 100 meV/unit cell window of configurations at 25 GPa. The response is larger at a higher defect concentration, although it does not exceed 0.07 eV at 25 GPa. Such a small predicted response coupled with $GeO_2$'s ultrawide band gap explains why no meaningful transport results were seen with our setup in the disordering region.

To evaluate if other phases could be responsible for the response observed in the x-ray data, several perturbed structures were optimized across 20–30 GPa including rutile supercells with single displaced oxygens, swapping the atomic positions between the known phases, and the known phases with small orthorhombic distortions. Nearly all of the perturbed structures revert to either the rutile or $CaCl_2$ phase when optimized. However, displacing an O in the *ab* plane within a single rutile unit cell leads to the orthorhombically distorted rutile structure mentioned earlier. The predicted orthorhombic distortion extends *a* and contracts *b* by similar amounts, $\sim$0.03 Å at 25 GPa. This orthorhombic phase has similar electronic properties to that of the rutile phase but is slightly more dense, leading to its predicted enthalpic favorability between 23 and 27.5 GPa [Fig. 1(b)]. As stated above, there is insufficient experimental evidence to validate this proposed phase, leaving the structure with a displaced oxygen atom as the leading model to explain the experimental observations.

Having established that distortions along the rutile phase's $B_{1g}$ librational mode leads to changes in the electronic structure of $GeO_2$, Fig. 5 contrasts the total charge density and electron localization function for a 25 GPa pristine rutile supercell and one where the single oxygen is displaced by $11°$ along the $B_{1g}$ librational mode with a 0.91% defect density. This point is marked with a black x in Fig. 4, and it was chosen because it is at the edge of the window of potentially accessible displacements with a $\Delta H$ of 101 meV/unit cell. Note that the octahedra in the $CaCl_2$ structure are rotated by
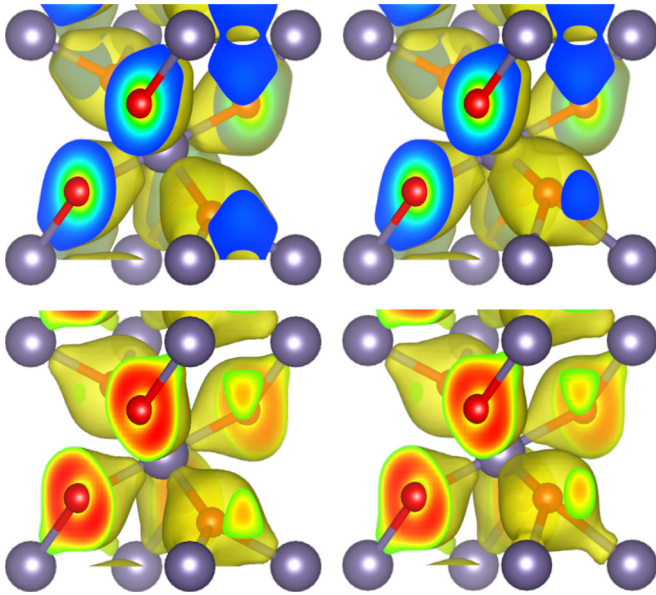
FIG. 5. (Top) The charge density with an isosurface level of 0.05 $e/a_0^3$ and (bottom) electron localization function with an isosurface level of 0.5 for a 25 GPa $3\times3\times3$ supercell of (left) pristine rutile GeO$_2$ and (right) rutile GeO$_2$ with a single $11°$ oxygen displacement as indicated in Fig. 4. Only one unit cell of the supercell is shown.
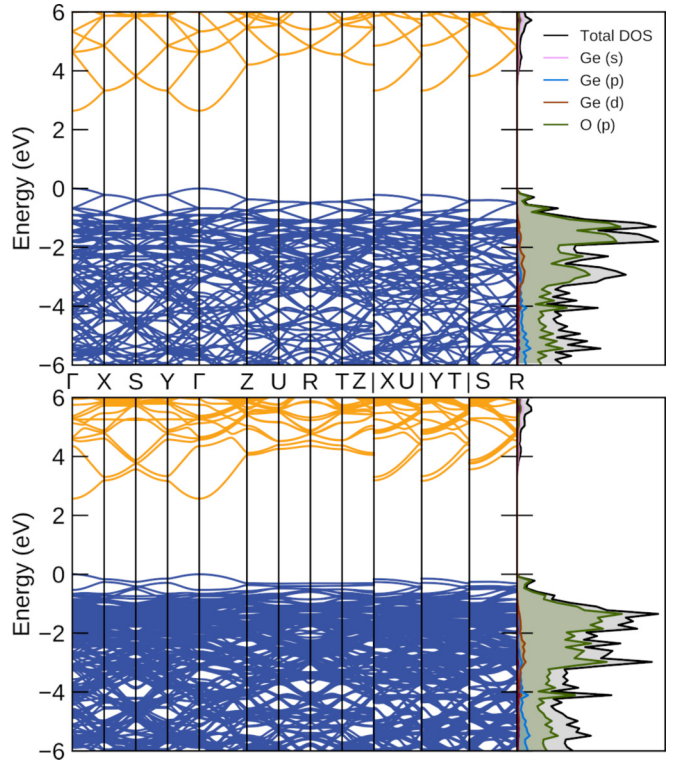


FIG. 6. The band structure and projected density of states for a 25 GPa $3\times3\times3$ supercell of (top) pristine rutile GeO$_2$ and (bottom) rutile GeO$_2$ with a single $11°$ oxygen displacement as indicated in Fig. 4.

$4°$ relative to the rutile structure. The charge density for the pristine rutile cell (Fig. 5, top left) shows a strongly polarized charge density about each oxygen atom with lobes in the direction of the Ge atoms with that oxygen in its basal plane, confirming the covalency inferred by bond lengths and their response to compression. When the oxygen atom is displaced (Fig. 5, top right), its charge density becomes more spherical while the charge density about the other oxygen atoms remain largely unperturbed. The electron localization function (ELF) of the rutile and displaced cell (Fig. 5, bottom) tell a similar story, where the distortion shifts towards an increased charge localization on the perturbed oxygen. Unlike the total charge density the distorted structure's ELF shows residual charge density (above the uniform electron gas limit) on the Ge atoms the oxygen moved away from. The atom projected charge density shows an accumulation of $0.04e$ of charge on the displaced oxygen, yet those neighboring Ge atoms with residual electron localization loose $0.1e$ of charge a piece. Thus the displacement involves metal-to-ligand charge transfer, yet the transferred charge density is more diffuse than the displaced oxygen's PAW sphere.

The band structure for a $3\times3\times3$ rutile GeO$_2$ supercell with a single displaced oxygen atom (Fig. 6) shows that most of the individual bands within the valence and conduction band don't alter much from the rutile phase beyond degeneracy breaking from the increased asymmetry of the disordered state. The curvature of the bands near the conduction band minimum (CBM) is largely unchanged by the disordering, looking primarily like spilt versions of the same bands. Near the valence band maximum (VBM), the split bands are flatter than their rutile counterparts. If the defect is propagated further, for instance with a $31°$ displacement in a $2\times2\times2$ supercell, those effect is far more prominent with three nearly

flatten bands comprising the VBM (plot in Ref. [35]). These changes in curvature of the VBM increase the effective hole mass of the material, in turn effecting several of the material's transport, optical, and electron-phonon related properties [41]. In particular, the increase in effective hole mass along with the mostly unchanged effective electron mass should increase conductivity in disordered rutile materials, although these simulations show the effect will depend heavily on the concentration and magnitude of disordering defects.

The flatter bands at the VBM of disordered rutile GeO$_2$ can indicate spatial localization, which the band decomposed charge density (Fig. 7) confirms to be the case even for the nearly rutile-like bands of the $11°$ displacement in a $3\times3\times3$ supercell. The VBM of the distorted rutile phase shows the formation of a small polaron composed of a polarized p state on the displaced oxygen with a strong coupling to p states on nearby oxygen atoms. This is in contrast to the VBM of the rutile phase which is a Bloch function of oxygen $p$ states. The formation of small polarons localized on the distorted oxygen atom is in line with the increase in the Ge K-edge energy observed when GeO$_2$ defects, in that charge density is localizing on the displaced oxygen and removing covalently shared density from the Ge. Polarons such as these have previously been observed in rutile materials via doping/vacancies [42–46] (including GeO$_2$) [16] or photoinduction [46,47]. Small polarons are known to facilitate electron transport via a hopping mechanism mediated through electron-phonon interactions [43,47,48], with a tunneling probability prefactor on the order of the phonon frequencies and an average rate
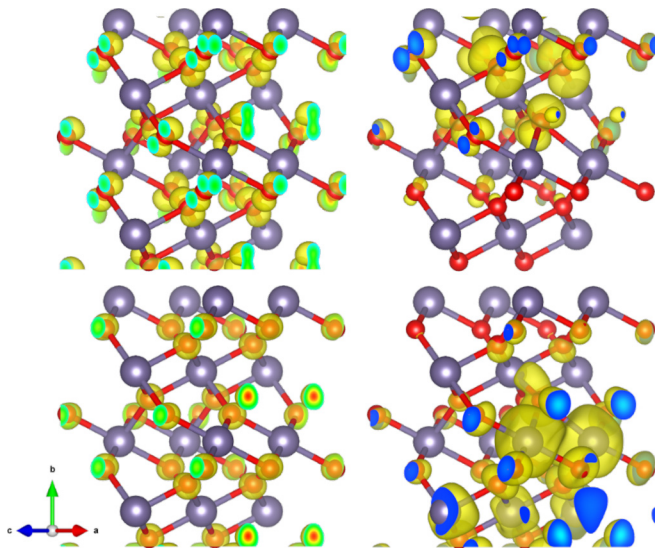
FIG. 7. Band decomposed charge densities for the (top) valence band maximum and (bottom) conduction band minimum for a 25 GPa $3\times3\times3$ supercell of (left) pristine rutile $GeO_2$ and (right) rutile $GeO_2$ with a single $11°$ oxygen displacement as indicated in Fig. 4. All isosurfaces are at 0.001 $e/a_0^3$ and show only the relevant portion of the supercell.

proportional to the polaron concentration [49]. Thus pressure inducing such defects offers an alternate means from doping to create small polarons in rutile materials to tune their electronic properties.

## IV. CONCLUSIONS

In conclusion, x-ray and Raman measurements confirm disordering in the oxygen sub-lattice of rutile $GeO_2$ just before the $CaCl_2$ phase transformation, providing further evidence for the universality of a disordered, pretransition state in rutile oxides. This pretransition, disordered state is driven by oxygen displacements arising from the softening $B_{1g}$ octahedral libration mode, with ion identity affecting the stability window for a disordered state. DFT simulations indicate that the disordering of an oxygen atom comes with an enthalpy penalty which also lowers the band gap of the material. The simulations also show the lowered band gap is due to an emerging flat band near the Fermi level in the disordered state which represent the formation of a small polaron about the displaced oxygen atom.

[1] F. Datchi, B. Mallick, A. Salamat, G. Rousse, S. Ninet, G. Garbarino, P. Bouvier, and M. Mezouar, Phys. Rev. B **89**, 144101 (2014).

[2] V. Prakapenka, G. Shen, L. Dubrovinsky, M. Rivers, and S. Sutton, J. Phys. Chem. Solids **65**, 1537 (2004).

[3] J. Haines, J. M. Léger, C. Chateau, and A. S. Pereira, Phys. Chem. Miner. **27**, 575 (2000).

[4] J. Haines and J. M. Léger, Phys. Rev. B **55**, 11144 (1997).

[5] J. Haines, J. M. Léger, and O. Schulte, J. Phys.: Condens. Matter **8**, 1631 (1996).

[6] J. Buchen, H. Marquardt, K. Schulze, S. Speziale, T. B. Ballaran, N. Nishiyama, and M. Hanfland, J. Geophys. Res.: Solid Earth **123**, 7347 (2018).

[7] A. Togo, F. Oba, and I. Tanaka, Phys. Rev. B **78**, 134106 (2008).

[8] A. E. Ringwood and M. Seabrook, J. Geophys. Res. (1896-1977) **68**, 4601 (1963).

[9] A. Ringwood, Geochim. Cosmochim. Acta **55**, 2083 (1991).

[10] J. Y. Tsao, S. Chowdhury, M. A. Hollis, D. Jena, N. M. Johnson, K. A. Jones, R. J. Kaplar, S. Rajan, C. G. Van de Walle, E. Bellotti, C. L. Chua, R. Collazo, M. E. Coltrin, J. A. Cooper, K. R. Evans, S. Graham, T. A. Grotjohn, E. R. Heller, M. Higashiwaki, M. S. Islam *et al.*, Adv. Electron. Mater. **4**, 1600501 (2018).

[11] M. Stapelbroek and B. Evans, Solid State Commun. **25**, 959 (1978).

[12] K. A. Mengle, S. Chae, and E. Kioupakis, J. Appl. Phys. **126**, 085703 (2019).

[13] J.-Y. Shin, S.-J. Kim, D.-K. Kim, and D.-H. Kang, Appl. Environ. Microbiol. **82**, 2 (2016).

[14] S. R. M. da Silva, G. K. Rolim, G. V. Soares, I. J. R. Baumvol, C. Krug, L. Miotti, F. L. Freire, M. E. H. M. da Costa, and C. Radtke, Appl. Phys. Lett. **100**, 191907 (2012).

[15] Y. Kamata, Mater. Today **11**, 30 (2008).

[16] S. Chae, J. Lee, K. A. Mengle, J. T. Heron, and E. Kioupakis, Appl. Phys. Lett. **114**, 102104 (2019).

[17] D. Smith, D. Sneed, N. Dasenbrock-Gammon, E. Snider, G. A. Smith, C. Childs, J. S. Pigott, N. Velisavljevic, C. Park, K. V. Lawler, R. P. Dias, and A. Salamat, J. Phys. Chem. Lett. **10**, 5351 (2019).

[18] D. Andrault, R. J. Angel, J. L. Mosenfelder, and T. Le Bihan, Am. Mineral. **88**, 301 (2003).

[19] A. Dewaele, M. Torrent, P. Loubeyre, and M. Mezouar, Phys. Rev. B **78**, 104102 (2008).

[20] B. Ravel and M. Newville, J. Synchrotron Radiat. **12**, 537 (2005).

[21] J. J. Rehr, J. J. Kas, M. P. Prange, A. P. Sorini, Y. Takimoto, and F. Vila, C. R. Phys. **10**, 548 (2009).

[22] Y. Li, W. Fan, H. Sun, X. Cheng, P. Li, X. Zhao, J. Hao, and M. Jiang, J. Phys. Chem. A **114**, 1052 (2010).

[23] W. Kohn and L. J. Sham, Phys. Rev. **140**, A1133 (1965).

[24] R. Sabatini, T. Gorni, and S. de Gir, Phys. Rev. B **87**, 041108(R) (2013).

[25] J. Sun, A. Ruzsinszky, and J. P. Perdew, Phys. Rev. Lett. **115**, 036402 (2015).

[26] H. Peng, Z.-H. Yang, J. P. Perdew, and J. Sun, Phys. Rev. X **6**, 041005 (2016).

[27] J. G. Brandenburg, J. E. Bates, J. Sun, and J. P. Perdew, Phys. Rev. B **94**, 115144 (2016).

[28] S. Grimme, J. Antony, S. Ehrlich, and H. Krieg, J. Chem. Phys. **132**, 154104 (2010).

[29] L. Goerigk and S. Grimme, Phys. Chem. Chem. Phys. **13**, 6670 (2011).

[30] J. D. Pack and H. J. Monkhorst, Phys. Rev. B **16**, 1748 (1977).

[31] P. E. Blöchl, O. Jepsen, and O. K. Andersen, Phys. Rev. B **49**, 16223 (1994).

[32] P. E. Blöchl, Phys. Rev. B **50**, 17953 (1994).

[33] K. Lejaeghere, G. Bihlmayer, T. Björkman, P. Blaha, S. Blügel, V. Blum, D. Caliste, I. E. Castelli, S. J. Clark, A. Dal Corso, S. de Gironcoli, T. Deutsch, J. K. Dewhurst, I. Di Marco, C. Draxl, M. Dułak, O. Eriksson, J. A. Flores-Livas, K. F. Garrity, L. Genovese *et al.*, Science **351**, aad3000 (2016).

[34] A. M. Ganose, A. J. Jackson, and D. O. Scanlon, J. Open Source Software **3**, 717 (2018).

[35] See Supplemental Material at http://link.aps.org/supplemental/10.1103/PhysRevB.104.134107 for XRD refinements and tabulated lattices, 1-shell model EXAFS fits, transport data, DFT predicted lattices and enthalpies, as well as additional simulation results for a $2\times2\times2$ supercell.

[36] A. Dewaele and P. Loubeyre, High Press. Res. **27**, 419 (2007).

[37] B. Cordero, V. Gómez, A. E. Platero-Prats, M. Revés, J. Echeverría, E. Cremades, F. Barragán, and S. a. Alvarez, Dalton Trans., 2832 (2008).

[38] S. Calvin, *XAFS for Everyone* (Taylor & Francis, Boca Raton, 2013).

[39] G. Bunker, *Introduction To XAFS: A Practical Guide to X-ray Absorption Fine Structure Spectroscopy* (Cambridge University Press, Cambridge, 2010).

[40] P. Fornasini, F. Monti, and A. Sanson, J. Synchrotron Radiat. **8**, 1214 (2001).

[41] R. H. Bube, *Electrons In Solids: An Introductory Survey*, 2nd ed. (Academic Press, Cambridge, Massachusetts, 1988).

[42] O. W. Johnson, W. D. Ohlsen, and P. I. Kingsbury, Phys. Rev. **175**, 1102 (1968).

[43] N. A. Deskins and M. Dupuis, Phys. Rev. B **75**, 195212 (2007).

[44] Y. Aoki and S. Saito, J. Phys.: Conf. Ser. **302**, 012034 (2011).

[45] L.-B. Mo, Y. Wang, Y. Bai, Q.-Y. Xiang, Q. Li, W.-Q. Yao, J.-O. Wang, K. Ibrahim, H.-H. Wang, C.-H. Wan, and J.-L. Cao, Sci. Rep. **5**, 17634 (2015).

[46] M. Reticcioli, U. Diebold, G. Kresse, and C. Franchini, in *Handbook of Materials Modeling: Applications: Current and Emerging Materials*, edited by W. Andreoni and S. Yip (Springer International Publishing, Cham, 2019), pp. 1–39.

[47] L. Zhang, W. Chu, C. Zhao, Q. Zheng, O. V. Prezhdo, and J. Zhao, J. Phys. Chem. Lett. **12**, 2191 (2021).

[48] J. Schnakenberg, Phys. Status Solidi (b) **28**, 623 (1968).

[49] S. Baranovskii and O. Rubel, in *Springer Handbook of Electronic and Photonic Materials*, edited by S. Kasap and P. Capper (Springer International Publishing, Cham, 2017), p. 1.